Journal of
Materials Chemistry B

ROYAL SOCIETY
OF CHEMISTRY

PAPER

View Article Online
View Journal | View Issue

Check for updates

Cite this: *J. Mater. Chem. B*, 2023, **11**, 8056

Published on 24 July 2023. Downloaded on 1/31/2026 12:10:10 AM.

Injectable, antibacterial, and oxygen-releasing chitosan-based hydrogel for multimodal healing of bacteria-infected wounds

Shayesteh Bochani,†[ab] Atefeh Zarepour,†[c] Ali Kalantari-Hesari,[d] Fakhri Haghi,[e] Mohammad-Ali Shahbazi,[fg] Ali Zarrabi,[c] Sophia Taheri[b] and Aziz Maleki *[hab]

Received 4th June 2023,
Accepted 21st July 2023

DOI: 10.1039/d3tb01278f

rsc.li/materials-b

Bacterial infection is one of the main challenges of wound healing. It imposes financial and healthcare costs. The emergence of antibiotic-resistant bacteria has increased concerns about this challenge, and made finding alternative solutions a crucial aim. We created a new, antibacterial, multifunctional hydrogel with synergistic chemodynamic and photothermal features for wound-healing applications. We fabricated a chitosan (CT)-based hydrogel containing tannic acid (TA), Fe, and MnO_2 nanosheets ($CT–TA–Fe–MnO_2$) *via* a simple method and characterized it. The antibacterial features (resulting from the production of reactive oxygen species within bacterial cells) and healing ability (*via* anti-inflammatory and hemostatic features) of the hydrogel were confirmed *in vitro*. *In vivo* results revealed the effectiveness of the $CT–TA–Fe–MnO_2$ hydrogel in decreasing the hemostatic time, improving anti-inflammatory effects, and promoting wound healing during 14 days by enhancing the deposition and maturation of collagen fibers without affecting the vital organs. The fabricated $CT–TA–Fe–MnO_2$ hydrogel could be a promising candidate with antibacterial and anti-inflammatory activities suitable for wound-healing applications.

Introduction

Each year, millions of wounds created by surgical procedures or trauma need to be managed. To reach an appropriate healing environment, open wounds need fast closure initially.[1] If a wound area is infected by bacteria, then the repair process will be hard. This is because inflammatory responses can lead to cell death and even tissue necrosis, thereby postponing wound healing significantly.[2] Many conventional antibiotics have been used to overcome bacterial infections, but bacterial resistance poses a big challenge.[3]

If bacteria gain access to a wound and grow within the wound area, hypoxia occurs, which further postpones wound healing.[4] It has been demonstrated that O_2 delivery to a wound site can accelerate cell proliferation and collagen synthesis, thus promoting tissue regeneration.[5–7] Therefore, the design and fabrication of a wound dressing with antibacterial and anti-inflammatory characteristics while supplying adequate oxygen are of vital importance for wound treatments.[8,9] Wound dressings have been developed as an important means of wound repair. Modern wound dressings composed of biological materials are employed by clinicians to overcome the shortcomings of traditional dressings. They maintain a wet and antibacterial environment around the wound and prompt wound healing. Dressings can be films, hydrogels, wafers, foams, and nanofibers. Hydrogels have garnered great attention in wound-healing applications.[2] Their porous structure possesses high mechanical properties, good absorption of water, biocompatibility and biodegradability. In addition, many therapeutic, photothermal and antibacterial agents can be loaded within hydrogels, endowing them with multifunctional properties.[10–12]

Chitosan (CT) is a nontoxic, biocompatible, biodegradable, and low-cost polysaccharide that has been used extensively in

---

[a] *Department of Pharmaceutical Nanotechnology, School of Pharmacy, Zanjan University of Medical Sciences, 45139-56184 Zanjan, Iran. E-mail: maleki@zums.ac.ir*
[b] *Zanjan Pharmaceutical Nanotechnology Research Center (ZPNRC), Zanjan, Iran*
[c] *Department of Biomedical Engineering, Faculty of Engineering and Natural Sciences, Istinye University, Istanbul 34396, Turkey*
[d] *Department of Pathobiology, Faculty of Veterinary Science, Bu-Ali Sina University, Hamadan, Iran*
[e] *Department of Microbiology, School of Medicine, Zanjan University of Medical Sciences, Zanjan, Iran*
[f] *Department of Biomedical Engineering, University Medical Center Groningen, University of Groningen, Antonius Deusinglaan 1, 9713 AV Groningen, The Netherlands*
[g] *W.J. Kolff Institute for Biomedical Engineering and Materials Science, University of Groningen, Antonius Deusinglaan 1, 9713 AV Groningen, The Netherlands*
[h] *Food and Drug Laboratory Research Center, Food and Drug Administration, MOH&ME, Tehran, Iran*

† Equally contributed to this work.

This journal is © The Royal Society of Chemistry 2023

Published on 24 July 2023. Downloaded on 1/31/2026 12:10:10 AM.

various biomedical applications.[13] Due to the hemostatic and antibacterial properties of CT-based hydrogels, they have the potential to promote wound regeneration.[14–19] Tannic acid (TA), a polyphenolic compound, contains groups of digallic acid which are conjugated to a central glucose core through ester bonds. TA has antioxidant, anti-inflammatory, antimicrobial, and antiviral properties.[20,21] TA can produce metal–tannic acid networks (MTNs) through chelation with metal ions. Such coordinative interactions can be used to engineer and fabricate functional MTNs to extend their potential applications in biomedical sciences.[20] Among various metal ions, complexation of TA with Fe^{3+} with low biotoxicity has received great attention.[22,23] Such organic–inorganic hybrid material has also exhibited excellent photothermal performance in the near-infrared (NIR) region.[24]

Chemodynamic therapy (CDT) is a promising approach to infection treatment. Use of nanostructures with nanozymes properties to convert hydrogen peroxide (H_2O_2) into the hydroxyl radical ($^{\bullet}OH$) has been undertaken. Using this method, minimum toxicity from the high concentrations of H_2O_2 in wound healing and higher antibacterial activity can be realized.[7,25] The reactive oxygen species (ROS) generated can destroy bacteria by damaging their cell wall, proteins, and DNA.[26] If CDT is combined with photothermal therapy (PTT), the killing efficiency can be improved further.[27] In PTT (implemented by NIR light and a photothermal agent), a high local temperature (>50 °C) can eradicate bacteria.[28] Manganese dioxide (MnO_2) nanosheets are a class of nanostructures. They can act as chemodynamic- and photothermal-active agents for bacterial killing.[29] However, only a few examples of MnO_2 nanosheet-incorporated hydrogels for wound-healing applications have been documented.[27,30,31] In addition, MnO_2 nanozymes can decompose H_2O_2 into O_2 to relieve oxidative stress, which is beneficial for wound-healing acceleration.[30,31] Although a combination of CT with TA as a hydrogel formulation (*e.g.*, carboxymethyl CT–TA,[32] CT–TA-oxidized hyaluronic acid,[33] CT–silver–TA,[34] quaternized CT–TA[35]) has been used in wound-healing applications, a combination of PTT, CDT, and oxygen delivery in a single formulation based on CT–TA has been overlooked.

Herein, we developed an injectable, antibacterial, hemostatic, and photothermally active hydrogel for accelerating wound repair (Fig. 1). The hydrogel was prepared by a facile and one-step approach by simple mixing of Fe–TA networks with CT polymer and subsequent mixing with MnO_2 nanosheets. The resulting hydrogel, named ''CT–TA–Fe–MnO_2'', showed excellent antibacterial activity *via* PTT and CDT. It produced oxygen, which is important in wound repair. Furthermore, TA and CT were introduced into the hydrogel to

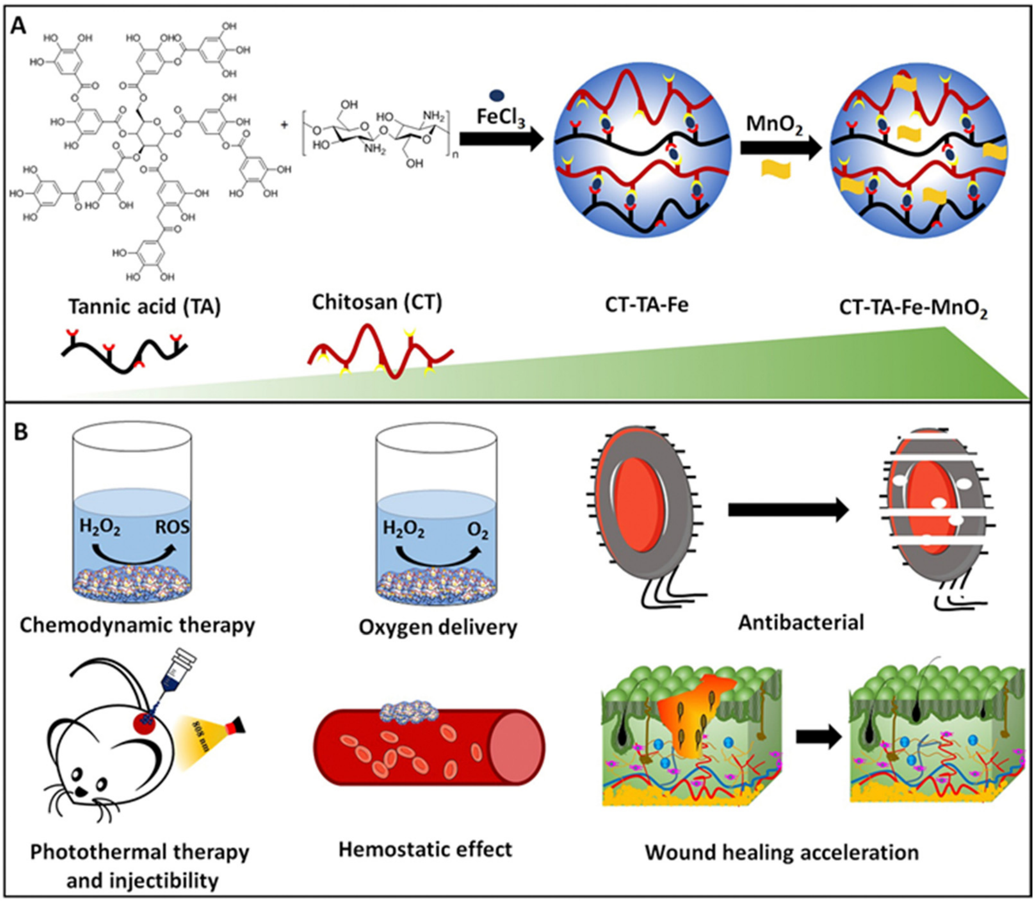

Fig. 1 (A) Preparation of a CT–TA–Fe–MnO_2 hydrogel (schematic). (B) Applications of the CT–TA–Fe–MnO_2 hydrogel.

Published on 24 July 2023. Downloaded on 1/31/2026 12:10:10 AM.

regulate the behavior of anti-inflammatory and hemostatic wound-healing processes through a synergistic effect. More importantly, applications of the CT–TA–Fe–MnO_2 hydrogel could significantly accelerate full-thickness wound healing according to histopathology studies.

Materials and methods

Sodium dodecyl sulfate (SDS; molecular weight (M_W) = 288.38 g mol^{-1}, Merck, Germany), potassium permanganate ($KMnO_4$; M_W = 158.034 g mol^{-1}, Merck, Germany), concentrated sulfuric acid (H_2SO_4), tannic acid (Merck, Germany), ferric chloride hexahydrate ($FeCl_3 \cdot 6H_2O$, Merck, Germany), Dulbecco's modified Eagle's medium (DMEM, Merck, Germany), CT (medium M_W = 190–310 kDa with deacetylation of 75–85%), penicillin/streptomycin (PenStrep, Sigma Aldrich), 3-[4,5-dimethylthiazole-2-yl]-2,5-diphenyltetrazolium bromide (MTT, Merck, Germany), foetal bovine serum (FBS, Merck, Germany), methylene blue (MB; M_W = 319.85, Merck, Germany), and brain heart infusion (BHI) broth/agar (Merck, Germany) were used.

Characterization

The size and morphology of samples were determined by transmission electron microscopy (TEM) using an EM208S system (Philips, the Netherlands), scanning electron microscopy (SEM) employing a Quanta 250 setup (FEG, USA), and atomic force microscopy (AFM) using a system from JPK Instruments (Germany). AFM was done based on intermittent contact (tapping) mode in which a silicon cantilever (Acta; APPNANO, USA) with a resonant frequency of ~300 kHz and nominal spring constant of 37 N m^{-1} was used. The scan rate and imaging resolution were 1.0 Hz and 512 × 512 pixels, respectively. The crystalline structure of samples was characterized by powder X-ray diffraction (PXRD) using a PW 1730 setup (Philips) employing a Cu-K_α radiation lamp and 2θ range of 5–85°. The chemical structure and surface functional groups of samples were determined using Fourier transform infrared (FTIR) spectroscopy using a spectrometer (IFS 66v/s; Bruker, Germany) in the wavenumber range of 400–4000 cm^{-1}. We wished to obtain deeper understanding of the effect of TA–Fe and MnO_2 nanosheets on the elasticity of hydrogel networks. Hence, the storage modulus (G') and loss modulus (G'') of each sample were measured using oscillatory rheology. This analysis was made based on parallel-plate geometry on a controlled-stress rotational rheometer (HAAKE™ MARS™ III; Thermo Scientific, USA).

Fabrication of single-layer MnO_2 nanosheets

Each two-dimensional (2D) MnO_2 nanosheet was synthesized using a single-step reduction method.[30] In brief, a mixture of SDS (32 mL, 0.1 M) and H_2SO_4 (1.6 mL, 0.1 M) in distilled water (280 mL) was prepared and mixed for 15 min at 96 °C. During heating, a $KMnO_4$ solution (0.05 M) was quickly added to the solution to produce a dark-brown homogenous solution. The final product was separated by centrifugation (10 000 rpm, 10 min) and washed with water and alcohol to obtain pure MnO_2 nanosheets.[36]

Preparation of the CT–TA–Fe–MnO_2 hydrogel

The CT–TA–Fe–MnO_2 hydrogel was fabricated through a facile mixing method. In brief, 5% (w/v) CT powder was dissolved in acetic acid solution (2% w/v) at room temperature and mixed for 12 h. Then, a solution of $FeCl_3$ (60 μL, 60 μg mL^{-1}) and TA (300 μL, 5% w/v) was added dropwise into the CT solution. The mixture was vortex-mixed at room temperature to obtain a CT–TA–Fe hydrogel. After that, 2D-MnO_2 nanosheets (500 μg mL^{-1}) were added to the CT–TA–Fe hydrogel to obtain the CT–TA–Fe–MnO_2 hydrogel. Different concentrations of sterilized CT–TA–Fe and CT–TA–Fe–MnO_2 were based on the concentration of the Fe ion and MnO_2 respectively.

Initial water content studies

After preparing the CT–TA–Fe–MnO_2 hydrogel, the initial wet weight was determined for all types of hydrogels. Then, samples were completely dried and their weights measured again to calculate the initial water content (IWC) using equation 1:

$$\text{IWC}\ (\%) = (W_g - W_s)/W_g \times 100 \tag{1}$$

where, W_g is the initial wet weight of the gel and W_s represents the weight of the sample after drying.

Photothermal effect of CT–TA–Fe and CT–TA–Fe–MnO_2

The photothermal activity of hydrogels (with/without MnO_2) was assessed by determining temperature changes in response to NIR irradiation. In this test, 1 mL of the as-prepared hydrogel was placed into a glass vial and exposed to an NIR laser (808 nm) at a power density of 0.5, 1.0, or 1.5 W cm^{-2} for 10 min. The local temperature was monitored dynamically using a digital thermal imager (TiS55; Fluke, USA).[37,38]

Detection of ROS and extracellular O_2 evaluation

Solutions of MB (1 μg mL^{-1}) and H_2O_2 (1 mM) were added to different concentrations of CT–TA–Fe or CT–TA–Fe–MnO_2 hydrogels and incubated for 30 min at 37 °C after exposure to NIR irradiation. The same process was followed for samples that were not exposed to irradiation. The effects of radical species on MB degradation were determined by measuring the absorbance of the solution at 665 nm.[39] To assess O_2 generation by CT–TA–Fe–MnO_2 and CT–TA–Fe, hydrogels were immersed in a H_2O_2 solution (1 mM) and the produced O_2 was measured using an oxygen meter (DO5510; Lutron, USA).[30]

In vitro antibacterial activity

First, to prepare sterilized hydrogels, we sterilized $FeCl_3$, TA, and CT powders under an ultraviolet lamp for 20 min before use. In addition, a bacteria culture medium was sterilized under a UV lamp for 30 min. The antibacterial efficacy of the hydrogels (CT–TA–Fe and CT–TA–Fe–MnO_2) were evaluated by counting the number of bacterial colonies.[40] *Staphylococcus aureus* ATCC 25923 and *Escherichia coli* ATCC 25922 were used as Gram-positive and Gram-negative bacterial models, respectively.

This journal is © The Royal Society of Chemistry 2023

Published on 24 July 2023. Downloaded on 1/31/2026 12:10:10 AM.

Then, 20 μL of bacterial suspension (0.5 McFarland) was added to 1 mL of different samples (saline (negative control), CT, CT–TA–Fe (+NIR irradiation), CT–TA–Fe (−NIR irradiation), CT–TA–Fe–MnO_2 (+NIR irradiation), and CT–TA–Fe–MnO_2 (−NIR irradiation)) and incubated for 1 h at 37 °C. Then, the solutions were diluted 30 times, cultured on nutrient agar, and incubated at 37 °C for 24 h. Next, the bacterial colonies in each group were counted to determine their antibacterial efficacy.[24] The minimum inhibitory concentration (MIC) of CT, CT–TA–Fe, and CT–TA–Fe–MnO_2 with and without irradiation with 808 nm light was determined using the broth-microdilution method.[41]

In vitro cell-viability assay

The cytocompatibility of hydrogels (CT–TA–Fe and CT–TA–Fe–MnO_2) was evaluated using mouse fibroblast (NIH-3T3) cells.[42] Briefly, 10×10^3 cells were cultured in each well of a 96-well plate in DMEM with 10% FBS and 1% PenStrep and incubated for 24 h at 37 °C in an atmosphere of 5% CO_2. Then, sterilized CT–TA–Fe or CT–TA–Fe–MnO_2 (250, 500, or 1000 μg mL^{-1}) were immersed in culture media and incubated for 24 h or 48 h at 37 °C. After incubation for 24 h or 48 h, cells were washed twice with phosphate-buffered saline (PBS). Then, 100 μL of pure media and 10 μL of MTT solution (in PBS at a concentration of 5 mg mL^{-1}) were added to each well followed by incubation for 4 h in the dark. Then, the medium in wells was replaced by DMSO followed by incubation for a further 1 h. Finally, the absorbance of wells at 570 nm was determined using a microplate reader (Infinite M200; Tecan, Austria). The percentage of viable cells was determined by comparing the results of each sample with negative-control wells (*i.e.*, cells treated with media only).

Animal treatment

The study protocol was approved (ZUMS.REC.1399.071) by the Zanjan University of Medical Sciences in Iran. Guidelines stated in the Guide for the Care and Use of Laboratory Animals by the US National Institutes of Medicine were adhered to. Male rats (200–220 g) were obtained from the Pasteur Institute (Iran). They were kept under standard laboratory conditions and had free access to water and food.

In vivo hemostatic performance of hydrogels

The hemostatic ability of hydrogels was evaluated using the rat-tail amputation model. Animals were divided into five groups of four. Rats were anesthetized. Half of the tail length was cut by surgical scissors. Then, the cut tail was covered with pre-weighted gauze and hemostatic freeze-dried hydrogels under slight pressure. Data on bleeding time and blood loss during the hemostatic process were recorded.[43,44]

In vivo wound healing, hemocompatibility, and histopathology

Sprague–Dawley rats (180–220 g) were divided into six groups of four. A full-thickness circular skin defect (diameter = 0.7 mm) was made on the back of each rat followed by infection with 20 μL of *S. aureus* (1×10^8 CFU mL^{-1}). Wounds were treated with PBS, CT–TA–Fe (−NIR irradiation), CT–TA–Fe (+NIR irradiation), CT–TA–Fe–MnO_2 (−NIR irradiation), CT–TA–Fe–MnO_2 (+NIR irradiation), or Tegaderm. Wounds were treated for 5 min with an NIR laser at a density of 1.5 W cm^{-2} for groups that underwent +NIR irradiation. Wounds were monitored daily. Images of the wounds were taken at days 0, 3, 7, and 14. Besides, regenerated skin tissues were removed on day 14 and sliced for staining (hematoxylin and eosin (H&E), periodic acid–Schiff (PAS), and Masson Trichrome) to evaluate the closure and regeneration of skin. Moreover, the effects of treatments on vital organs (liver, kidneys, and spleen) were tested by harvesting their vital organs for histology. Organs were first fixed in a 10% formaldehyde solution overnight, dehydrated, embedded in melted paraffin, mounted on a microtome, and cut into thin slices for H&E staining and visualization under optical microscopy (Bx51; Olympus, Japan) using DinoCapture v2 (Dinolite, USA).

Results and discussion

Characterization of MnO_2 nanosheets, CT–TA–Fe hydrogel, and CT–TA–Fe–MnO_2 hydrogel

The fabrication mechanisms of CT–TA–Fe and CT–TA–Fe–MnO_2 composite hydrogels are briefly demonstrated in Fig. 1. The CT–TA–Fe composite hydrogel was formed *via* interaction between the OH groups of CT and TA with Fe(III) cations. Addition of MnO_2 nanosheets to this structure created new crosslinking bonds by electrostatic interaction between the phenolic hydroxyl groups of TA and functional groups of CT chains with 2D-nanosheets (Fig. 2(A)).[30] TEM of MnO_2 nanosheets showed ultrathin nanosheets with average lateral size of ∼250 nm. (Fig. 2(B)). AFM revealed that MnO_2 nanosheets had a size and height of about 250 nm and 7 nm, respectively (Fig. 2(C)).[31] TEM and AFM confirmed fabrication of ultrathin MnO_2 nanosheets with size in the nano range. FT-IR spectroscopy was carried out to confirm the interactions among CT, TA, Fe ions, and 2D-MnO_2 nanosheets (Fig. 2(D)). In the CT spectrum, a broad band in the range of 3000–3500 cm^{-1} represented N–H and O–H stretching, as well as intramolecular hydrogen bonding. The absorption bands centred at 2921 and 2877 cm^{-1} were attributed to C–H symmetric and asymmetric stretching, respectively. These features could have been related to the polysaccharide-specific bands of CT.[15] The existence of residual *N*-acetyl groups was confirmed by bands at ∼1645 cm^{-1} (C═O stretching of amide I) and 1325 cm^{-1} (C–N stretching of amide III), respectively.[45] In the case of TA, phenolic –OH stretching vibration peaks were observed at 3000–3600 cm^{-1}.[15] The peaks originating from the stretching vibrations of C═O (carboxylic ester) groups of TA appeared at 1704 cm^{-1}. Besides, characteristic peaks at 1500 to 1600 cm^{-1} were due to stretching vibrations of the benzene moieties of TA.[46,47] In the FT-IR spectrum of $FeCl_3$, a broad band at ∼3400 cm^{-1} might have been related to the hydroxyl group of the water molecules of $FeCl_3$.[48] Mn–O and Mn–O–Mn vibrations appeared at ∼400–600 cm^{-1} in the spectra of MnO_2.[49] The bending and stretching vibrations of water molecules or O–H groups in the interlayer

Published on 24 July 2023. Downloaded on 1/31/2026 12:10:10 AM.

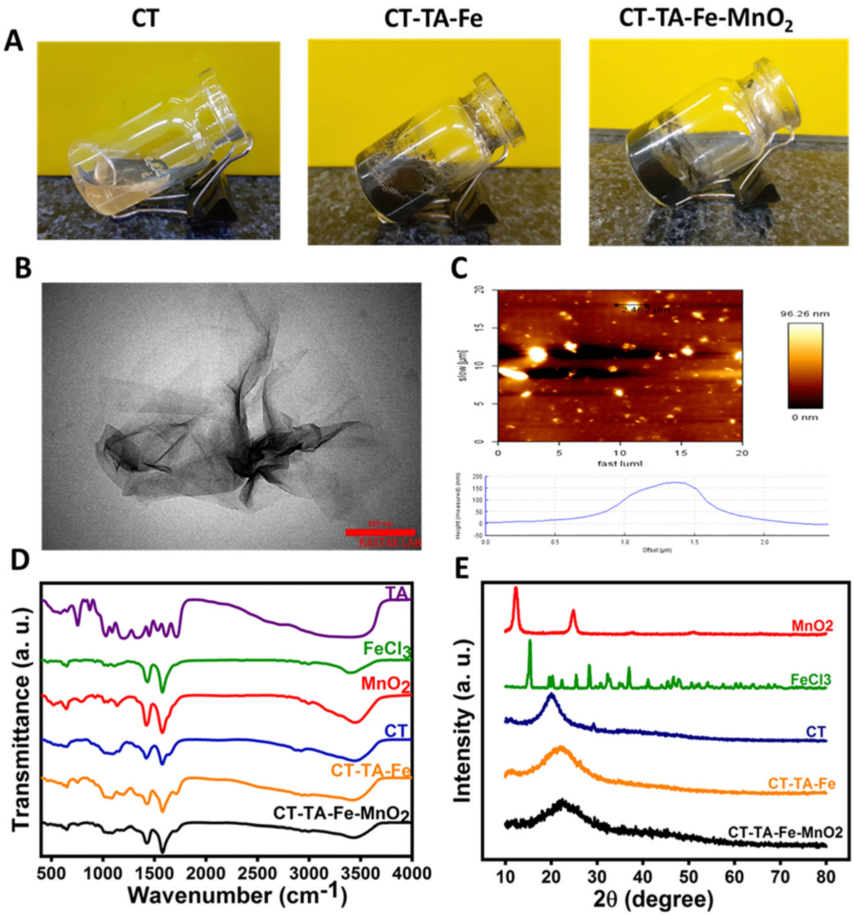

Fig. 2 (A) Photographs of CT, CT–TA–Fe, and CT–TA–Fe–MnO$_2$. (B) TEM image of MnO$_2$ nanosheets (scale bar = 200 nm). (C) AFM image of MnO$_2$ sheets. (D) FT-IR spectra and (E) XRD pattern of CT, FeCl$_3$, CT–TA–Fe, MnO$_2$, and CT–TA–Fe–MnO$_2$.

space of the MnO$_2$ nanosheets were responsible for the bands that appeared at 1577 and 3446 cm^{-1}.[36,50] In the FT-IR spectrum of CT–TA–Fe and CT–TA–Fe–MnO$_2$, a decrease in the vibration peaks of phenolic–OH and stretching of benzene rings was observed, which could have been related to the coordinative interaction between Fe and TA/CT as well as the electrostatic interaction of the MnO$_2$ nanosheets with the hydrogel network.[47,51–53] XRD analysis was employed to determine the crystalline structure of CT-based hydrogels (Fig. 2(D)). CT powder showed a broad characteristic peak at 2θ = 20°, indicating the amorphous structure of this polymer.[54] FeCl$_3$ peaks were observed at 2θ = 21.2°, 33.3°, and 34.1°.[55] The XRD profile of the resulting MnO$_2$ nanosheets showed peaks at 2θ = 12.3°, 24.3°, 36.6°, and 66.2°, which correspond to the peaks of δ-MnO$_2$.[36] As shown in Fig. 1(E), the sharp peaks of FeCl$_3$ and MnO$_2$ disappeared in the diffractogram of CT–TA–Fe and CT–TA–Fe–MnO$_2$ hydrogels, respectively, which confirmed the interaction between CT, Fe ions, and MnO$_2$ nanosheets and fabrication of an amorphous hydrogel.[15,27]

The morphology of the CT–TA–Fe–MnO$_2$ hydrogel was further examined using SEM: it exhibited a porous network structure (Fig. 3(A)).[56] This porous structure could influence hydrogel properties such as compressibility,[57] swelling,[58] cell adhesion,[59] and nutrient diffusion.[60] Energy-dispersive X-ray spectroscopy (EDS) confirmed uniform dispersion of Mn and Fe ions in the structure of the CT–TA–Fe–MnO$_2$ hydrogel (Fig. 3(B)). The initial water content of all three types of hydrogels (CT, CT–TA–Fe, and CT–TA–Fe–MnO$_2$) was nearly the same (∼85%), revealing that the presence of Fe, TA, or MnO$_2$ nanosheets did not have any effect on the water content of hydrogels (Fig. 3(C)). The viscoelastic properties of CT, CT–TA–Fe, and CT–TA–Fe–MnO$_2$ hydrogels were determined using rheology employing oscillatory shear strain at ∼0.5% and an angular frequency between 0.01 and 100 Hz. The amount of G' was substantially greater than G'' in all groups (Fig. 3(D) and (E)), indicating the elasticity of the produced hydrogels.[61] Besides, the amount of G' in the CT–TA–Fe hydrogel and its MnO$_2$ nanosheet-reinforced form was higher than that of CT alone, which implied that these hydrogels had more rigid and stable network systems (Fig. 3(F)). In addition, the viscoelastic moduli of both hydrogels were frequency-independent, demonstrating the rheological behavior of the gel-like material (Fig. 3(F)). The storage modulus CT–TA–Fe and CT–TA–Fe–MnO$_2$ was higher than that of CT, showing the lower stiffness of CT than that of the hydrogels (Fig. 3(G)). Moreover, the injectability of CT–TA–Fe–MnO$_2$ was tested by injection

Published on 24 July 2023. Downloaded on 1/31/2026 12:10:10 AM.

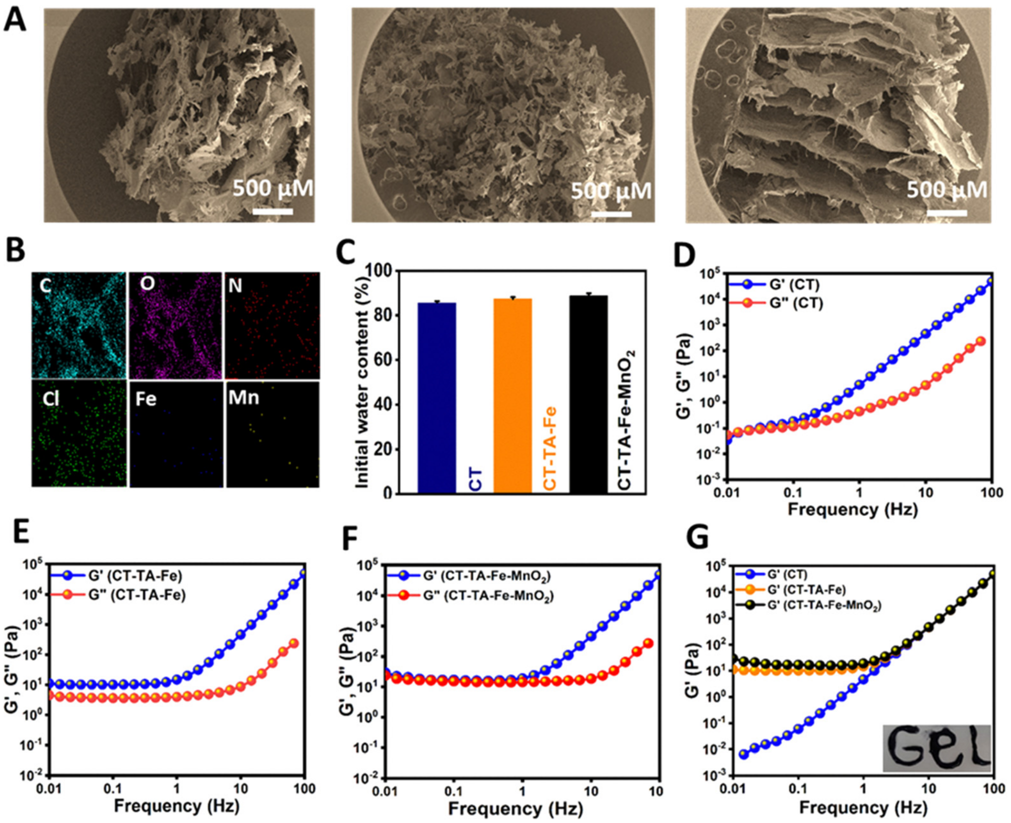

Fig. 3 (A) SEM images of CT, CT–TA–Fe, and CT–TA–Fe–MnO_2. (B) Energy-dispersive spectroscopy (EDS) mapping images of CT–TA–Fe–MnO_2. (C) Initial water content of hydrogels. (D)–(F) Storage modulus (G') and loss modulus (G'') of CT, CT–TA–Fe, and CT–TA–Fe–MnO_2 *versus* frequency (Hz) (*G*) Storage modulus of CT, CT–TA–Fe, and CT–TA–Fe–MnO_2; inset shows injectable properties of CT–TA–Fe–MnO_2.

with a 20-G needle, indicating that the hydrogel had reversible thixotropic properties (Fig. 3(G), inset).

In vitro photothermal activity, chemodynamic property, and evaluation of extracellular O_2 of CT–TA–Fe and CT–TA–Fe–MnO_2

Recently, PTT and CDT have gained popularity due to their high therapeutic efficacy and non-invasive nature over conventional therapeutic systems.[62–64] MnO_2 nanosheets having broad NIR absorption have assured "light-responsive" potential to generate spatial- and temporal-regulated hyperthermia for enhanced PTT.[65] Along with PTT, CDT utilizes transition metal-containing nanoparticles, such as MnO_2 nanosheets, to induce intracellular oxidative stress by converting the less reactive H_2O_2 into $^{\bullet}OH$ through a Fenton-like reaction.[66,67] CT–TA–Fe–MnO_2 hydrogels were fabricated to achieve all three modalities in a single platform by taking advantage of the synergy of PTT, CDT, and oxygen delivery to a wound. Using the same amount of CT, CT–TA–Fe, and CT–TA–Fe–MnO_2 hydrogels, CT–TA–Fe–MnO_2 was used to evaluate their photothermal effect. As indicated in Fig. 4(A), the temperature of CT, CT–TA–Fe, and CT–TA–Fe–MnO_2 hydrogels reached to 23.7, 41.5, and 50.5 °C after 10 min irradiation, respectively. Besides, the temperature of CT–TA–Fe–MnO_2 showed a stable on–off behaviour after five cycles of NIR illumination and free cooling continuous irradiation (Fig. 4(B)). Fig. 4(C) displays the thermal images of CT–TA–Fe and CT–TA–Fe–MnO_2 hydrogels exposed to 808 nm light continuously for 10 min. Thermal images demonstrated a time-dependent effect for the NIR activity of hydrogels. Moreover, the temperature increase was much higher in the CT–TA–Fe–MnO_2 hydrogel in comparison with the CT–TA–Fe hydrogel. The crucial step in CDT is $^{\bullet}OH$ generation by the Fenton reaction, which was evaluated utilizing MB as an indicator in the presence and absence of NIR light.[68] As shown in Fig. 4(D), a negligible amount of MB was degraded when it was mixed with H_2O_2 and CT–TA–Fe, whereas clear degradation occurred when CT–TA–Fe–MnO_2 was mixed with H_2O_2 solution. This effect was increased further when an NIR laser was used, confirming that local hyperthermia accelerated the rate of the Fenton-like reaction, thus endowing the CT–TA–Fe–MnO_2 hydrogel with high chemodynamic activity.[27] Next, we evaluated the oxygen-production capability of the CT–TA–Fe–MnO_2 hydrogel using a portable dissolved-oxygen meter. Fig. 4(E) shows that that CT–TA–Fe–MnO_2 had catalase-like activity that could accelerate O_2 production when it was mixed with H_2O_2. CT–TA–Fe mixed with H_2O_2 also had a moderate capability of oxygen production, but it was much lower than that of the CT–TA–Fe–MnO_2 hydrogel. These results suggested that MnO_2 nanosheets and Fe could act as active centers for catalase-like activity.[69]

Published on 24 July 2023. Downloaded on 1/31/2026 12:10:10 AM.

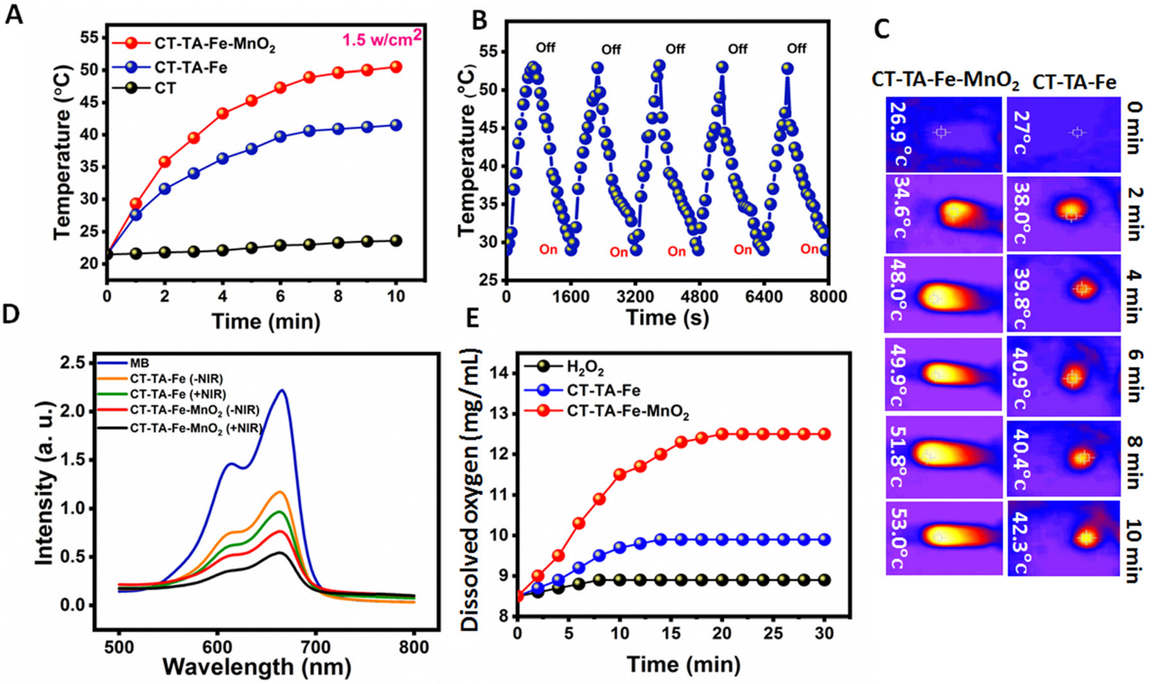

Fig. 4 (A) Photothermal properties of CT, CT–TA–Fe, and CT–TA–Fe–MnO_2 hydrogels (500 μg mL^{-1}) under 808 nm laser irradiation with a power density of 1.5 W cm^{-2}. (B) Temperature *vs.* time curve for CT–TA–Fe–MnO_2 (500 μg mL^{-1}) irradiated with an 808 nm laser (1.5 W cm^{-2}) for five on–off cycles (on: 10 min; off: 10 min). (C) NIR thermal images of CT–TA–Fe and CT–TA–Fe–MnO_2 under 808 nm laser irradiation at different times. (D) UV-vis spectrum of MB after different treatments with CT–TA–Fe and CT–TA–Fe–MnO_2 hydrogels with/without NIR light. (E) Oxygen release by CT–TA–Fe and CT–TA–Fe–MnO_2 hydrogels in the presence of H_2O_2 measured by a commercial oxygen meter.

In vitro antibacterial activity of hydrogels

When a wound is healing, bacterial infection becomes a big problem. Thus, antibacterial agents have significant roles during the healing process.[70] *E. coli* and *S. aureus* were chosen as Gram-negative and Gram-positive bacteria, respectively, to investigate the antibacterial activity of different samples in the presence/absence of NIR light (Fig. 5(A)). The CT group showed negligible antibacterial activity even in the presence of light. In the case of CT–TA–Fe and CT–TA–Fe–MnO_2 hydrogels and in the absence of NIR, significant activity against *S. aureus* was noted, but they could not completely inhibit the growth of *E. coli* and some colonies remained. In this case, the CT–TA–Fe–MnO_2 hydrogel was more effective than the CT–TA–Fe hydrogel, and the number of colonies created on the plate of this sample was less than that of the sample without MnO_2. This antibacterial activity could have resulted from the nanozyme activity of MnO_2 nanosheets and Fe^{+3}. That is, Fe^{+3} could absorb bacteria by interacting with their negatively charged membrane, and then MnO_2 nanosheets destroyed them by producing ROS components such as $^{\bullet}OH$. NIR irradiation could enhance the antibacterial capability of both hydrogels so that they completely inhibited the growth of bacteria (Fig. 5(B) and (C)).[27] NIR irradiation led to temperature enhancement of ~42 °C and ~50 °C for CT–TA–Fe and CT–TA–Fe–MnO_2, respectively. Such hyperthermia could boost the antibacterial effect of the multifunctional hydrogels (Fig. 5(D)).[10,69] The MIC of different samples (CT, CT–TA–Fe, and CT–TA–Fe–MnO_2 with/without NIR irradiation) was calculated. The NIR-treated CT–TA–Fe–MnO_2 hydrogel had a MIC of 0.03 and 0.06 μg mL^{-1} against *E. coli* and *S. aureus*, respectively. CT–TA–Fe–MnO_2 and CT–TA–Fe hydrogels without NIR irradiation had the same MIC values (0.03 and 0.10 μg mL^{-1}) against *E. coli* and *S. aureus*, respectively, in the dilutions we evaluated. These results indicated that permeation of the bacterial membrane was increased by light irradiation and the bacterial membrane was penetrated more readily by ROS. Hence, the proteins in the bacterium were severely depleted, which caused the bacteria to die.[40]

In vitro cell viability

High cytocompatibility is a vital feature for hydrogels used in wound healing.[71] Therefore, the cytocompatibility of CT–TA–Fe and CT–TA–Fe–MnO_2 hydrogels was investigated using the MTT assay. NIH-3T3 cells treated with different concentrations of CT–TA–Fe or CT–TA–Fe–MnO_2 hydrogels had high viability even at a high concentrations (up to 1000 μg mL^{-1}) (Fig. 6(A) and (B)). Besides, at a high concentration, they could enhance cell viability, and cell viability was enhanced to >100%, thus confirming the cytocompatibility of the hydrogels. This increased cell viability could be attributed to the ions released (Fe^{3+} and Mn^{2+}) from hydrogels, which promoted the proliferation and migration of cells. It has been shown that the intracellular delivery of Fe ions can lead to beneficial biological effects, such as gene expression and cell migration.[72] It has been reported that the treatment of fibroblasts with Mn ions can increase focal cell adhesion and the binding affinity of integrins with the extracellular matrix.[73]

Published on 24 July 2023. Downloaded on 1/31/2026 12:10:10 AM.

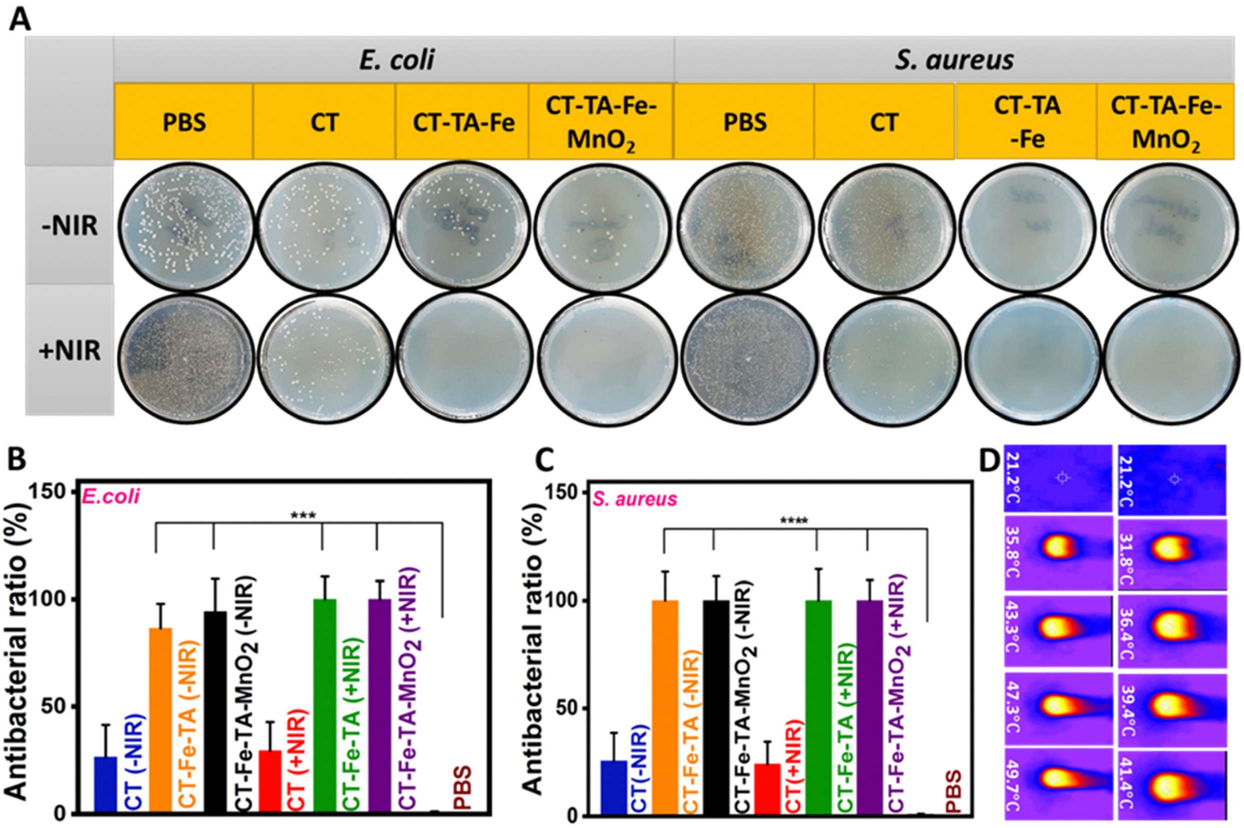

Fig. 5 Antibacterial performance. (A) Viable bacterial colonies on plates after treatment with PBS, CT, CT–TA–Fe, or CT–TA–Fe–MnO_2 with/without irradiation. (B) and (C) Antibacterial ratio (%) of different samples with/without NIR light. (D) Images of different hydrogel solutions under continuous NIR irradiation (1.5 W cm^{-2}) for 10 min (left column: CT–TA–Fe–MnO_2; right column: CT–TA–Fe). Independent tests were conducted three time for each group (***$p < 0.0007$, ****$p < 0.0001$).

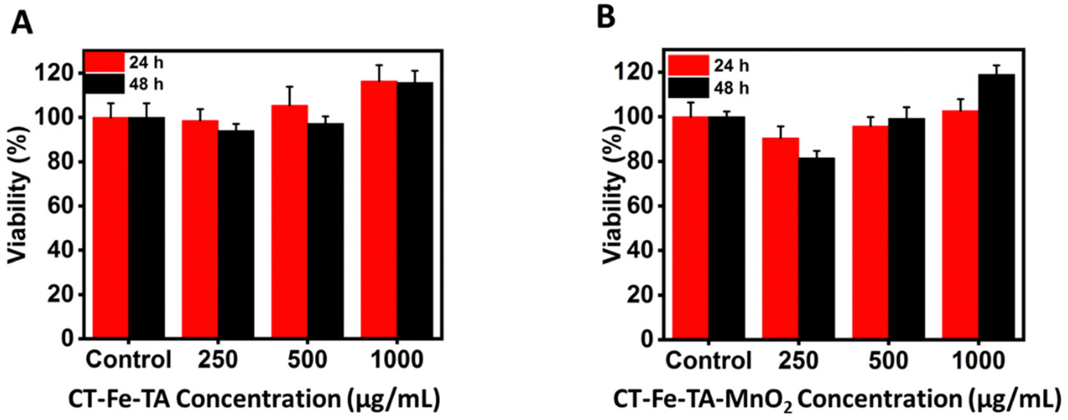

Fig. 6 Cell viability of different concentrations of CT–TA–Fe and CT–TA–Fe–MnO_2 hydrogels against NIH-3T3 cells at 24 h (A) and 48 h (B).

In vivo blood-clot experiments

The first step in wound healing is hemostasis. Therefore, hemostatic agents that can stop bleeding quickly are essential for wound healing or to save time for additional treatment.[43,74] A hemostatic model based on an amputated rat tail was used to evaluate the hemostatic performance of hydrogels. We investigated the effects of hydrogels, as anti-bleeding agents, on blood loss and the time needed for hemostasis ("hemostatic time") (Fig. 7(A)). The hemostatic agents gauze, CT–TA–Fe, and CT–TA–Fe–MnO_2 hydrogels could significantly decrease the blood loss from 186 mg (control) to 127, 85, and 58 mg, respectively, ($p < 0.001$) (Fig. 7(B)). The hemostatic time for gauze, CT–TA–Fe, and CT–TA–Fe–MnO_2 hydrogels was 216, 175, and 70 s, respectively. These results demonstrated that

Published on 24 July 2023. Downloaded on 1/31/2026 12:10:10 AM.

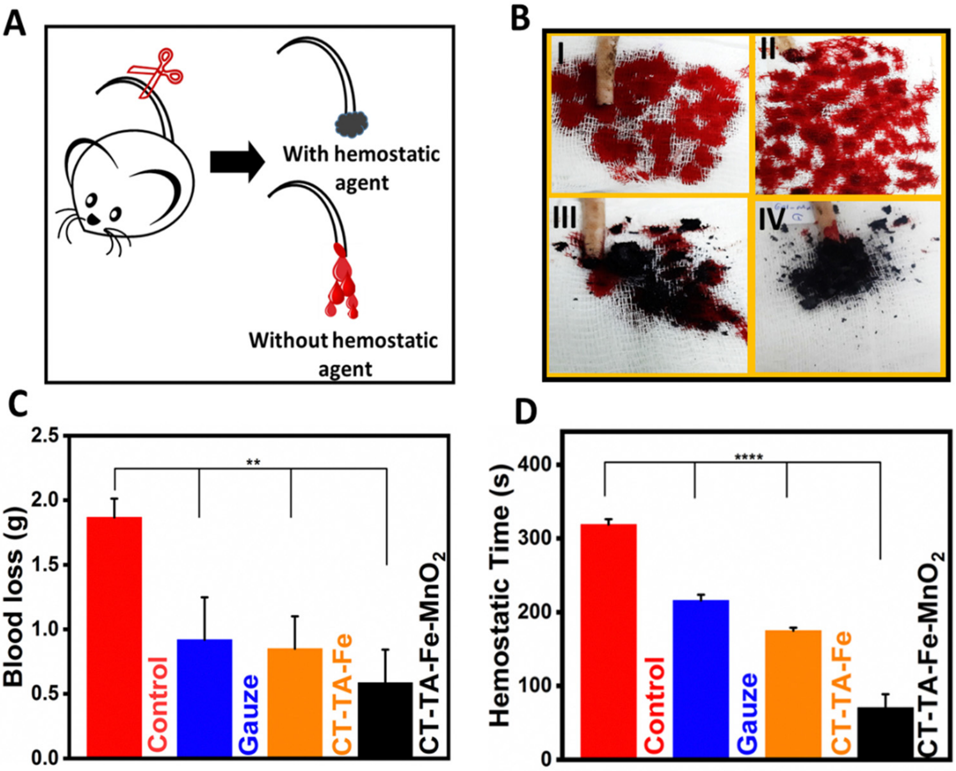

Fig. 7 *In vivo* and *in vitro* hemostatic performance of hydrogels. (A) Anti-bleeding studies in a rat tail-amputation model (schematic). (B) Hemostatic photographs (I: control; II: gauze; III: CT–TA–Fe; IV: CT–TA–Fe–MnO_2), (C) quantitative results of blood loss, and (D) hemostatic time using different treatments in a rat-tail model (n = 4; **** $p < 0.0001$, ** $p < 0.0012$).

the CT–TA–Fe–MnO_2 hydrogel was a better hemostatic agent than the current commercial type of gauze and the CT–TA–Fe hydrogel. This phenomenon could be related to the presence of positively charged Fe ions, Mn ions and the CT polymer that

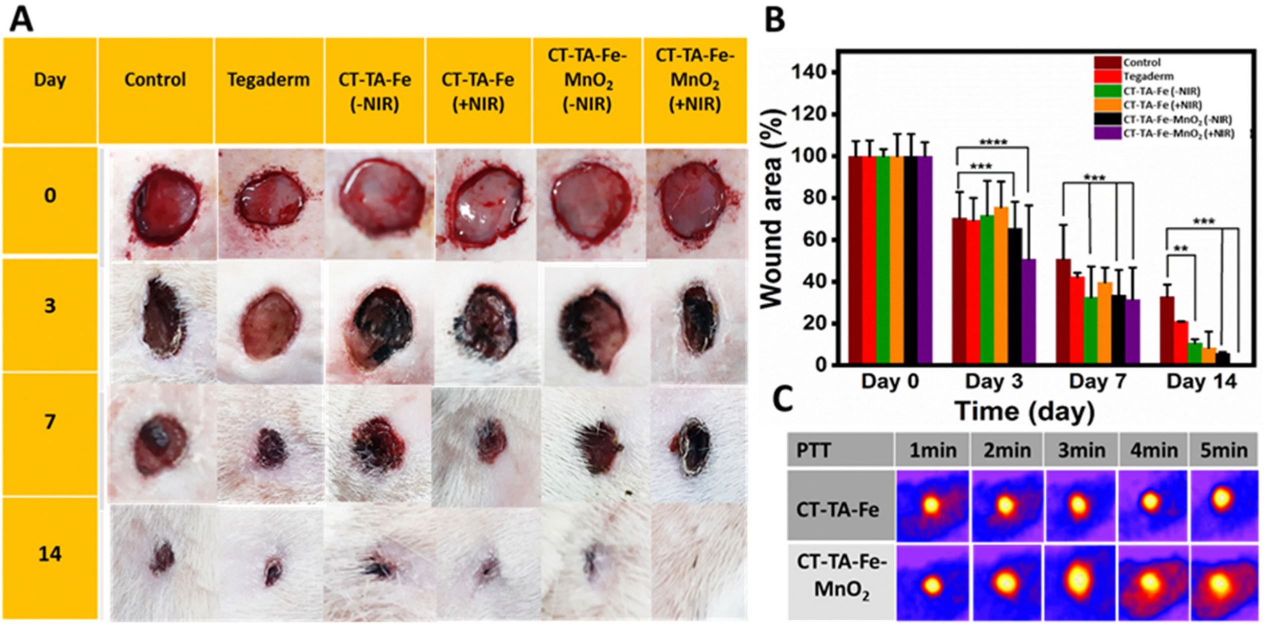

Fig. 8 *In vivo* wound healing of hydrogels. (A) Wound contraction during 14 days using PBS, Tegaderm, CT–TA–Fe (with/without NIR irradiation), or CT–TA–Fe–MnO_2 (with/without NIR irradiation) as a dressing (schematic). (B) Changes in wound size after different times (n = 5; ****$p < 0.0001$; error bars indicate mean ± standard deviation). (C) Real-time *in vivo* infrared thermal images of different treatments under 808 nm light irradiation.

Published on 24 July 2023. Downloaded on 1/31/2026 12:10:10 AM.

interact with blood cells and platelets *via* electrostatic interaction in the wound area.[44,74,75]

In vivo studies and histology

A full-thickness wound was created in Sprague–Dawley rats, and they were used as *in vivo* models to evaluate the wound-healing capability of CT–TA–Fe and CT–TA–Fe–MnO_2 hydrogels. Animals were divided into six groups: PBS (control), Tegaderm film, CT–TA–Fe (with/without NIR irradiation) and CT–TA–Fe–MnO_2 (with/without NIR irradiation). Control and Tegaderm groups demonstrated delayed wound recovery, as evidenced by digital pictures of the wound area and measurements of the relative area of wound that remained unrepaired after 14 days screening (Fig. 8(A)). CT–TA–Fe–MnO_2 was more effective than CT–TA–Fe, especially if the hydrogel was treated by NIR irradiation, so that it could heal the wound nearly

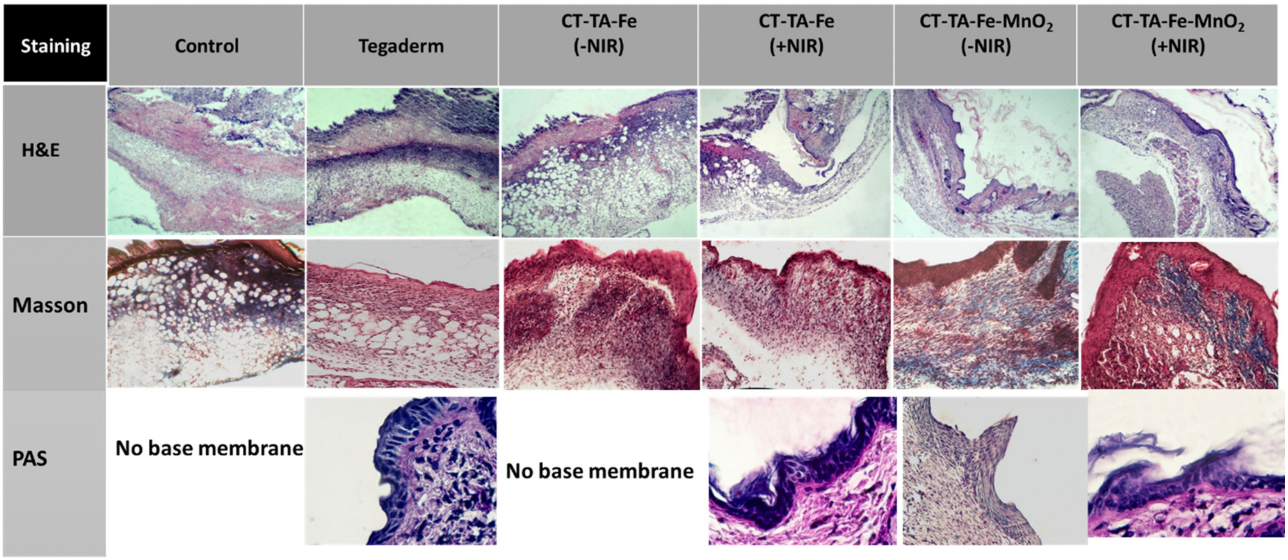

Fig. 9 Staining (H&E, Masson, and PAS) of healed skin tissues after 14 days.

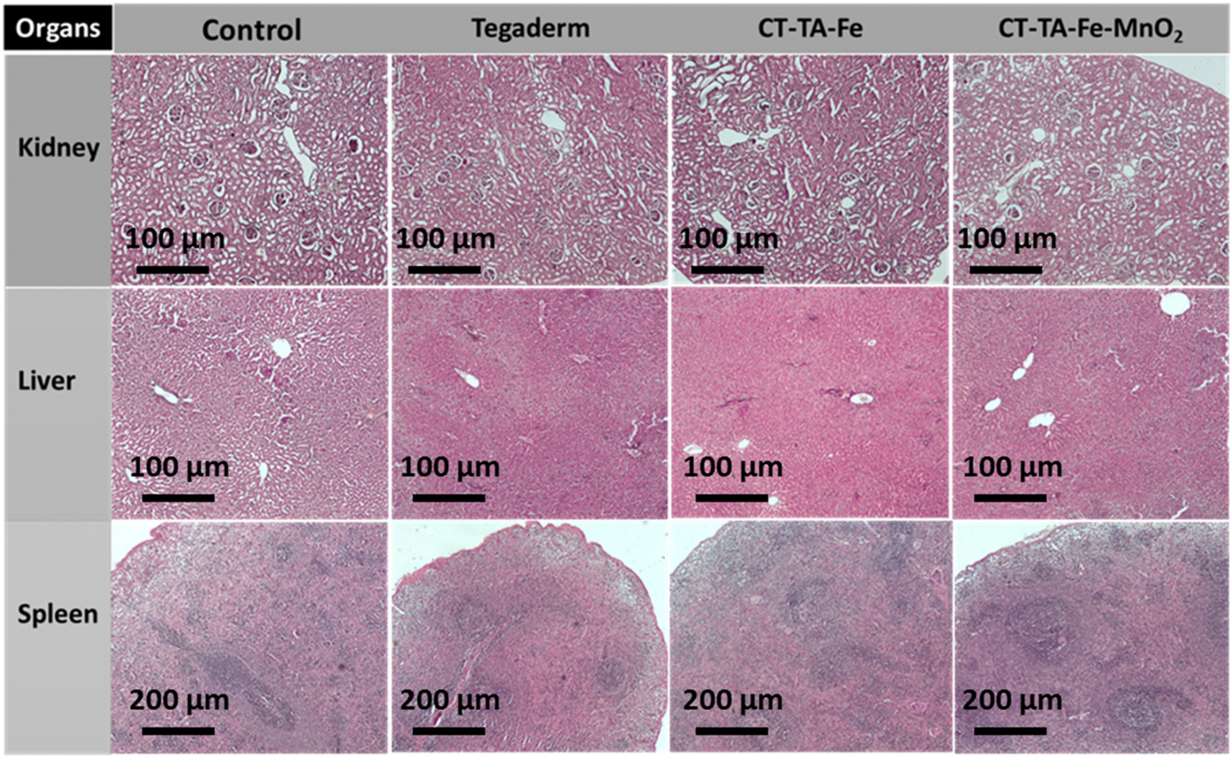

Fig. 10 Micrographs of H&E-stained tissue slices of major organs (liver, kidneys, and spleen) from different groups after 14 days of treatment.

Published on 24 July 2023. Downloaded on 1/31/2026 12:10:10 AM.

completely after 14 days. Wound photographs taken at various time intervals were used to compute wound areas and wound closure quantitatively (Fig. 8(B)). Quantitative data confirmed the better performance of the fabricated hydrogels against the wound in comparison with the commercial type. Real-time *in vivo* infrared thermal images of different treatments under 808 nm light irradiation were taken at various times with thermal digital camera (Fig. 8(C)). Compared with the CT–TA–Fe hydrogel, the CT–TA–Fe–MnO_2 hydrogel exhibited a greater increase in temperature, data which were in agreement with *in vitro* results. Hydrogels was used once when measuring the healing process.

Different histopathological tests were used to evaluate the effect of the hydrogels on the healing process using different treatments.[76] On day 14, the best regeneration of the epidermis and dermis, and a thicker hypoderm, was observed in the CT–TA–Fe–MnO_2 (+NIR irradiation) group according to H&E staining (Fig. 9). In comparison, the control and Tegaderm groups exhibited poor regeneration of epidermal and dermal tissue. Masson's trichrome staining was applied to depict the deposition and organization of collagen fibers during wound repair (Fig. 9). Staining showed deposition of dense collagen fibers and alignment in the defects treated by the CT–TA–Fe–MnO_2 hydrogel. The other groups showed poor deposition of collagen fibers. Lack of a basement membrane in the wound site in the control group on day 14 was shown by PAS staining. The basement membrane was clearly observed in the CT–TA–Fe–MnO_2 (+NIR irradiation) group (Fig. 9). Accelerated wound healing has been proposed to be due to the excellent antibacterial ability stemming from the release of Mn and Fe ions,[77] oxygen-release property of hydrogels, anti-inflammatory property of TA,[27] and creation of a moist environment for tissue regeneration by absorbing tissue exudate by CT-based hydrogels.[78] After 14 days of treatment, histology of vital organs (liver, spleen, and kidneys) in each group showed no abnormalities (Fig. 10), suggesting that the fabricated hydrogels were safe ''theragenerative'' materials for the acceleration of wound healing.

Conclusions

A new type of wound-healing hydrogel with intrinsic antibacterial features was introduced. MnO_2 nanosheets were synthesized and mixed with TA, $FeCl_3$, and CT to fabricate hydrogels. Different characteristics of the hydrogel and its different components (morphology, rheological features, chemical bonds, crystalline structure, water content, photothermal ability, and oxygen generation) were evaluated *via* physicochemical analysis. Besides, the antibacterial activity, cytocompatibility and wound-healing capability of the fabricated hydrogel were evaluated *in vitro* and *in vivo*. We fabricated nanosheets with a mean size of 250 nm, height of 7 nm, and crystalline structure. Physicochemical tests confirmed the fabrication of hydrogels (CT–TA–Fe–MnO_2 and CT–TA–Fe) with improved stability. The photothermal activity of the hydrogels in response to 808 nm irradiation was confirmed, and they exhibited stable on–off behavior after five NIR-irradiation and cooling cycles. In addition to a photothermal effect, the CT–TA–Fe–MnO_2 hydrogel showed chemodynamic activity by producing $^{\bullet}OH$ *via* a Fenton-like reaction. Moreover, the hydrogels had catalase-like activity and produced oxygen from H_2O_2 components. The fabricated hydrogels also had antibacterial activity against both Gram-positive and Gram-negative bacterial strains *via* generation of ROS components. Finally, *in vivo* tests showed the effectiveness of the photoactive hydrogels in healing wounds. In all cases, the CT–TA–Fe–MnO_2 hydrogel had better performance, even in comparison with the available commercial wound healing mat (Tegaderm). The TA–Fe–MnO_2 hydrogel could be a good candidate for wound-healing applications.

Conflicts of interest

There are no conflicts of interest to declare.

Acknowledgements

This work was supported by the Iran National Science Foundation (no. 99015911) and Food and Drug Administration, MOH & ME, Tehran, Iran (grant no. Pr983902).

References

1 G. Han and R. Ceilley, *Adv. Ther.*, 2017, **34**, 599.
2 Y. Liang, J. He and B. Guo, *ACS Nano*, 2021, **15**, 12687.
3 A. L. Hook, C. Y. Chang, J. Yang, S. Atkinson, R. Langer, D. G. Anderson, M. C. Davies, P. Williams and M. R. Alexander, *Adv. Mater.*, 2013, **25**, 2542.
4 J. I. Kang, K. M. Park and K. D. Park, *J. Ind. Eng. Chem.*, 2019, **69**, 397.
5 T. Agarwal, M. Costantini, S. Pal and A. Kumar, *J. Mater. Chem. B*, 2022, **10**, 7905.
6 Z. Wang, F. Rong, Z. Li, W. Li, K. Kaur and Y. Wang, *Chem. Eng. J.*, 2023, **452**, 139297.
7 Y. Li, R. Fu, Z. Duan, C. Zhu and D. Fan, *Bioact. Mater.*, 2022, **9**, 461.
8 A. Sood, R. Bhaskar, S. Y. Won, Y. J. Seok, A. Kumar and S. S. Han, *J. Nanostruct. Chem.*, 2022, **1**, DOI: 10.1007/s40097-022-00505-1.
9 L. G. Ding, S. Wang, B. J. Yao, F. Li, Y. A. Li, G. Y. Zhao and Y. B. Dong, *Adv. Healthcare Mater.*, 2021, **10**, 2001821.
10 A. Maleki, J. He, S. Bochani, V. Nosrati, M. A. Shahbazi and B. Guo, *ACS Nano*, 2021, **15**, 18895.
11 P. Atienza-Roca, D. C. Kieser, X. Cui, B. Bathish, Y. Ramaswamy, G. J. Hooper, A. N. Clarkson, J. Rnjak-Kovacina, P. J. Martens, L. M. Wise and T. B. Woodfield, *Biomater. Sci.*, 2020, **8**, 5005.
12 M. Villiou, J. I. Paez and A. Del Campo, *ACS Appl. Mater. Interfaces*, 2020, **12**, 37862.

This journal is © The Royal Society of Chemistry 2023

Published on 24 July 2023. Downloaded on 1/31/2026 12:10:10 AM.

13 M. C. Pellá, M. K. Lima-Tenório, E. T. Tenório-Neto, M. R. Guilherme, E. C. Muniz and A. F. Rubira, *Carbohydr. Polym.*, 2018, **196**, 233.

14 Y. Xiang, C. Mao, X. Liu, Z. Cui, D. Jing, X. Yang, Y. Liang, Z. Li, S. Zhu, Y. Zheng, K. W. K. Yeung, D. Zheng, X. Wang and S. Wu, *Small*, 2019, **15**, 1900322.

15 S. Guo, Y. Ren, R. Chang, Y. He, D. Zhang, F. Guan and M. Yao, *ACS Appl. Mater. Interfaces*, 2022, **14**, 34455.

16 Q. Xu, L. Zhang, Y. Liu, L. Cai, L. Zhou, H. Jiang and J. Chen, *J. Nanostruct. Chem.*, 2022, 1.

17 Y. Ou and M. Tian, *J. Mater. Chem. B*, 2021, **9**, 7955.

18 X. Wang, R. Song, M. Johnson, Z. He, C. Milne, X. Wang, I. Lara-Sáez, Q. Xu and W. Wang, *Materials*, 2021, **14**, 5956.

19 X. Wang, R. Song, M. Johnson, P. Shen, N. Zhang, I. Lara-Sáez, Q. Xu and W. Wang, *Macromol. Biosci.*, 2023, 2300094.

20 Z. Guo, W. Xie, J. Lu, X. Guo, J. Xu, W. Xu, Y. Chi, N. Takuya, H. Wu and L. Zhao, *J. Mater. Chem. B*, 2021, **9**, 4098.

21 A. Bigham, V. Rahimkhoei, P. Abasian, M. Delfi, J. Naderi, M. Ghomi, F. D. Moghaddam, T. Waqar, Y. N. Ertas, S. Sharifi and N. Rabiee, *Chem. Eng. J.*, 2022, **432**, 134146.

22 M. He, C. Du, J. Xia, Z. G. Zhang and C. M. Dong, *Biomacromolecules*, 2022, **23**, 2655.

23 Y. Ju, J. Cui, M. Müllner, T. Suma, M. Hu and F. Caruso, *Biomacromolecules*, 2015, **16**, 807.

24 T. Liu, M. Zhang, W. Liu, X. Zeng, X. Song, X. Yang, X. Zhang and J. Feng, *ACS Nano*, 2018, **12**, 3917.

25 J. Shan, X. Li, K. Yang, W. Xiu, Q. Wen, Y. Zhang, L. Yuwen, L. Weng, Z. Teng and L. Wang, *ACS Nano*, 2019, **13**, 13797.

26 J. Shan, K. Yang, W. Xiu, Q. Qiu, S. Dai, L. Yuwen, L. Weng, Z. Teng and L. Wang, *Small*, 2020, **16**, 2001099.

27 S. Bochani, A. Kalantari-Hesari, F. Haghi, V. Alinezhad, H. Bagheri, P. Makvandi, M.-A. Shahbazi, A. Salimi, I. Hirata, V. Mattoli, A. Maleki and B. Guo, *ACS Appl. Bio Mater.*, 2022, **5**, 4435.

28 M. Xu, Y. Hu, Y. Xiao, Y. Zhang, K. Sun, T. Wu, N. Lv, W. Wang, W. Ding, F. Li, B. Qiu and J. Li, *ACS Appl. Mater. Interfaces*, 2020, **12**, 50260.

29 T. Du, S. Chen, J. Zhang, T. Li, P. Li, J. Liu, X. Du and S. Wang, *Nanomaterials*, 2020, **10**, 1545.

30 S. Wang, H. Zheng, L. Zhou, F. Cheng, Z. Liu, H. Zhang and Q. Zhang, *Biomaterials*, 2020, **260**, 120314.

31 S. Wang, H. Zheng, L. Zhou, F. Cheng, Z. Liu, H. Zhang, L. Wang and Q. Zhang, *Nano Lett.*, 2020, **20**, 5149.

32 X. Zhou, Q. Zhou, Q. Chen, Y. Ma, Z. Wang, L. Luo, Q. Ding, H. Li and S. Tang, *ACS Biomater. Sci. Eng.*, 2023, **9**, 437.

33 S. Liu, N. Jiang, Y. Chi, Q. Peng, G. Dai, L. Qian, K. Xu, W. Zhong and W. Yue, *ACS Biomater. Sci. Eng.*, 2022, **8**, 3754.

34 G. Xu, N. Xu, T. Ren, C. Chen, J. Li, L. Ding, Y. Chen, G. Chen, Z. Li and Y. Yu, *Int. J. Biol. Macromol.*, 2022, **208**, 760.

35 W. Pan, X. Qi, Y. Xiang, S. You, E. Cai, T. Gao, X. Tong, R. Hu, J. Shen and H. Deng, *Int. J. Biol. Macromol.*, 2022, **195**, 190.

36 Z. Liu, K. Xu, H. Sun and S. Yin, *Small*, 2015, **11**, 2182.

37 S. Huang, H. Liu, K. Liao, Q. Hu, R. Guo and K. Deng, *ACS Appl. Mater. Interfaces*, 2020, **12**, 28952.

38 G. Gao, Y. W. Jiang, H. R. Jia and F. G. Wu, *Biomaterials*, 2019, **188**, 83.

39 B. Ma, S. Wang, F. Liu, S. Zhang, J. Duan, Z. Li, Y. Kong, Y. Sang, H. Liu, W. Bu and L. Li, *J. Am. Chem. Soc.*, 2019, **141**, 849.

40 C. Mao, Y. Xiang, X. Liu, Y. Zheng, K. W. K. Yeung, Z. Cui, X. Yang, Z. Li, Y. Liang, S. Zhu and S. Wu, *ACS Appl. Mater. Interfaces*, 2019, **11**, 17902.

41 Z. S. Aziz, S. Albukhaty and H. K. Abbood, *Karbala Int. J. Mod. Sci.*, 2017, **3**, 259.

42 K. Wang, J. Wang, L. Li, L. Xu, N. Feng, Y. Wang, X. Fei, J. Tian and Y. Li, *Chem. Eng. J.*, 2019, **372**, 216.

43 K. Quan, G. Li, L. Tao, Q. Xie, Q. Yuan and X. Wang, *ACS Appl. Mater. Interfaces*, 2016, **8**, 7666.

44 X. Zhao, B. Guo, H. Wu, Y. Liang and P. X. Ma, *Nat. Commun.*, 2018, **9**, 2784.

45 M. F. Queiroz, K. R. Teodosio Melo, D. A. Sabry, G. L. Sassaki and H. A. O. Rocha, *Mar. Drugs*, 2015, **13**, 141.

46 N. Sahiner, S. Sagbas, M. Sahiner and S. Demirci, *Polym. Degrad. Stab.*, 2016, **133**, 152.

47 N. Ninan, A. Forget, V. P. Shastri, N. H. Voelcker and A. Blencowe, *ACS Appl. Mater. Interfaces*, 2016, **8**, 28511.

48 M. A. Inam, R. Khan, D. R. Park, Y. W. Lee and I. T. Yeom, *Water*, 2018, **10**, 418.

49 X. Meng, L. Lu and C. Sun, *ACS Appl. Mater. Interfaces*, 2018, **10**, 16474.

50 X. Yang, Y. Makita, Z.-H. Liu, K. Sakane and K. Ooi, *Chem. Mater.*, 2004, **16**, 5581.

51 Laxmi, S. Khan, A. Kareem, F. Zafar and N. Nishat, *Spectrochim. Acta, Part A*, 2018, **188**, 400.

52 J. Yang, M. Li, Y. Wang, H. Wu, T. Zhen, L. Xiong and Q. Sun, *Biomacromolecules*, 2019, **20**, 801.

53 Y. Yang, W. Yan and C. Jing, *Langmuir*, 2012, **28**, 14588.

54 J. W. Rhim, S. I. Hong, H. M. Park and P. K. W. Ng, *J. Agric. Food Chem.*, 2006, **54**, 5814.

55 S. Zhou, K. You, H. Gao, R. Deng, F. Zhao, P. Liu, Q. Ai and H. Luo, *Mol. Catal.*, 2017, **433**, 91.

56 X. H. Wang, F. Song, D. Qian, Y. D. He, W. C. Nie, X. L. Wang and Y. Z. Wang, *Chem. Eng. J.*, 2018, **349**, 588.

57 S. L. Edwards, J. S. Church, D. L. J. Alexander, S. J. Russell, E. Ingham, J. A. M. Ramshaw and J. A. Werkmeister, *Tissue Eng., Part C*, 2011, **17**, 123.

58 B. Guo, A. Finne-Wistrand and A. C. Albertsson, *Biomacromolecules*, 2011, **12**, 2601.

59 J. Y. Lai and Y. T. Li, *Biomacromolecules*, 2010, **11**, 1387.

60 C. Ji, A. Khademhosseini and F. Dehghani, *Biomaterials*, 2011, **32**, 9719.

61 S. H. Kim, Y. K. Yeon, J. M. Lee, J. R. Chao, Y. J. Lee, Y. B. Seo, M. T. Sultan, O. J. Lee, J. S. Lee, S. I. Yoon and I. S. Hong, *Nat. Commun.*, 2018, **9**, 1620.

62 G. Liu, J. Zou, Q. Tang, X. Yang, Y. Zhang, Q. Zhang, W. Huang, P. Chen, J. Shao and X. J. Dong, *ACS Appl. Mater. Interfaces*, 2017, **9**, 40077.

63 C. Zhang, K. Zhao, W. Bu, D. Ni, Y. Liu, J. Feng and J. Shi, *Angew. Chem., Int. Ed.*, 2015, **54**, 1770.

Published on 24 July 2023. Downloaded on 1/31/2026 12:10:10 AM.

64 J. Xu, P. Yang, M. Sun, H. Bi, B. Liu, D. Yang, S. Gai, F. He and J. Lin, *ACS Nano*, 2017, **11**, 4133.

65 Z. Liu, S. Zhang, H. Lin, M. Zhao, H. Yao, L. Zhang, W. Peng and Y. Chen, *Biomaterials*, 2018, **155**, 54.

66 B. Ma, S. Wang, F. Liu, S. Zhang, J. Duan, Z. Li, Y. Kong, Y. Sang, H. Liu, W. Bu and L. Li, *J. Am. Chem. Soc.*, 2018, **141**, 849.

67 Z. Tang, Y. Liu, M. He and W. Bu, *Angew. Chem., Int. Ed.*, 2019, **131**, 958.

68 T. Li, J. Zhou, L. Wang, H. Zhang, C. Song, J. M. de la Fuente, Y. Pan, J. Song, C. Zhang and D. Cui, *Adv. Healthcare Mater.*, 2019, **8**, 1900192.

69 L. S. Lin, J. Song, L. Song, K. Ke, Y. Liu, Z. Zhou, Z. Shen, J. Li, Z. Yang, W. Tang and G. Niu, *Angew. Chem., Int. Ed.*, 2018, **130**, 4996.

70 W. Cassandra, *Nature*, 2017, **543**, 15.

71 E. Y. Jeon, B. H. Hwang, Y. J. Yang, B. J. Kim, B.-H. Choi, G. Y. Jung and H. J. Cha, *Biomaterials*, 2015, **67**, 11.

72 M. Wlaschek, K. Singh, A. Sindrilaru, D. Crisan and K. Scharffetter-Kochanek, Medicine, *Free Radicals Biol. Med.*, 2019, **133**, 262–275.

73 S. Munevar, Y. L. Wang and M. Dembo, *J. Cell Sci.*, 2004, **117**, 85–92.

74 B. Guo, R. Dong, Y. Liang and M. Li, *Nat. Rev. Chem.*, 2021, **5**, 773.

75 Y. Yang, Y. Liang, J. Chen, X. Duan and B. Guo, *Bioact. Mater.*, 2022, **8**, 341.

76 X. Zhou and B. B. Moore, *Bio-Protoc.*, 2017, **7**, e2286.

77 H. Li, P. Xia, S. Pan, Z. Qi, C. Fu, Z. Yu, W. Kong, Y. Chang, K. Wang, D. Wu and X. Yang, *Int. J. Nanomed.*, 2020, 7199.

78 Z. Xu, S. Han, Z. Gu and J. Wu, *Adv. Healthcare Mater.*, 2020, **9**, 1901502.

This journal is © The Royal Society of Chemistry 2023